

Gravity Waves in Global High-Resolution Simulations With Explicit and Parameterized Convection

C. C. Stephan¹, C. Strube², D. Klocke³, M. Ern², L. Hoffmann², P. Preusse², and H. Schmidt¹

¹Max Planck Institute for Meteorology, Hamburg, Germany, ²Forschungszentrum Jülich, Jülich, Germany,

³Hans-Ertel-Zentrum für Wetterforschung, Deutscher Wetterdienst, Offenbach, Germany

Key Points:

- Parameterized convection reduces the stratospheric zonal-mean zonal gravity wave momentum flux
- Explicit convection is associated with stronger updrafts and gravity wave sources
- Spectral changes result from more variable precipitation in the simulation with explicit convection

Correspondence to:

C. C. Stephan,
claudia.stephan@mpimet.mpg.de

Citation:

Stephan, C. C., Strube, C., Klocke, D., Ern, M., Hoffmann, L., Preusse, P., & Schmidt, H. (2019). Gravity waves in global high-resolution simulations with explicit and parameterized convection. *Journal of Geophysical Research: Atmospheres*, 124, 4446–4459. <https://doi.org/10.1029/2018JD030073>

Received 28 NOV 2018

Accepted 29 MAR 2019

Accepted article online 8 APR 2019

Published online 29 APR 2019

Abstract Increasing computing resources allow us to run weather and climate models at horizontal resolutions of 1–10 km. At this range, which is often referred to as the convective gray zone, clouds and convective transport are partly resolved, yet models may not achieve a satisfactory performance without convective parameterizations. Meanwhile, large fractions of the gravity wave (GW) spectrum become resolved at these scales. Convectively generated GWs are sensitive to spatiotemporal characteristics of convective cells. This raises the question of how resolved GWs respond to changes in the treatment of convection. Two global simulations with a horizontal grid spacing of 5 km are performed, one with explicit and one with parameterized convection. The latitudinal profiles of absolute zonal-mean GW momentum flux match well between both model configurations and observations by satellite limb sounders. However, the simulation with explicit convection shows ~30–50% larger zonal-mean momentum fluxes in the summer hemisphere subtropics, where convection is the dominant source of GWs. Our results imply that changes in convection associated with the choice of explicit versus parameterized convection can have important consequences for resolved GWs, with broad implications for the circulation and the transport in the middle atmosphere.

1. Introduction

Gravity waves (GWs) are important for driving the circulation and transport in the middle and upper atmosphere and contribute to the exchange of constituents between the troposphere and the stratosphere. GWs are mainly generated by orography (Lott & Miller, 1997; McFarlane, 1987), jets and fronts (Plougonven & Zhang, 2014), and convection (Piani et al., 2000; Song & Chun, 2005; Stephan & Alexander, 2015). The grid spacing required for an explicit simulation of the full GW spectrum would need to be fine enough to resolve individual convective updrafts. Therefore, contemporary general circulation models (GCMs) use parameterizations for GWs, and there exist several methods for specifying the GW spectra from different sources. Convective sources dominate GW generation in the tropics and subtropics, whereas jets, fronts, and orography dominate in the midlatitudes. By tuning the independent GW source parameterizations separately, it is therefore possible to tweak specific components of the atmospheric circulation system (e.g., Garcia et al., 2017; Orr et al., 2010). In this sense GW parameterizations have been an important tool for achieving realistic large-scale circulation patterns in GCMs.

Convective cells, in particular, are underresolved, even at grid spacings of 1 km. Therefore, subgrid convective processes are themselves often parameterized. Schemes for convective parameterizations implicitly assume that the dynamical scale of the convection is significantly smaller than a grid box. With increasing computational capacities, global models are now starting to run at resolutions of a few kilometers. These grid spacings are still coarser than the cloud scale but finer than the intercloud separation scale. Since neither traditional parameterization schemes nor explicit dynamics are well suited to this intermediate regime, it is commonly referred to as the gray zone (Prein et al., 2015).

At fine resolutions, GWs, too, can be treated in multiple ways. The 7-km GEOS-5 Nature Run (Gelaro & Coauthors, 2015), for instance, still used a parameterization for orographic GWs, and despite having a realistic generation of nonorographic GWs, their parameterization was necessary due to excessive dissipation of the waves (Holt et al., 2017). Different setups are also used for simulations at resolutions much coarser than the convective scale. In experiments discussed in Geller et al. (2013), the Kanto model with a 62.5-km

resolution near the equator (Watanabe et al., 2008), for example, did not use any GW parameterization but achieved a realistic circulation through very little dissipation at small scales. In the CAM5 simulation (Bacmeister et al., 2014) with a 25.5-km resolution near the equator, described in Geller et al. (2013), only orographic GWs were parameterized. These examples hint at the challenges that will be encountered when GCM resolutions approach the gray zone. Without GW parameterizations, important tuning parameters are lost. As the experience with the Nature Run shows, it cannot be taken for granted that the generation of resolved waves is realistic and that their drag forces result in the desired atmospheric circulation. Convectively generated GWs may pose a particular problem, as their implementation in GCMs may rely on two parameterizations building on top of each other (e.g., Beres et al., 2005; Choi & Chun, 2011; Kim et al., 2013; Richter et al., 2010).

However, even when the resolution of the model is sufficient to resolve a large fraction of the GWs considered, the use of a convective parameterization has a strong influence on the excited GWs (Kim et al., 2007; Preusse et al., 2014). Müller et al. (2018) showed that a convective parameterization inhibited the generation of GWs by convection. They argued that this was due to a lack of variance in latent heating at small scales and due to a lack of deep heating. However, their sensitivity test was based on an idealized zonally symmetric aqua planet model without rotation and no background winds. Therefore, it is of high interest to consider how global GW distributions may change in a start-of-the-art GCM when all convective parameterizations are turned off.

This study seeks to assess how the properties of resolved GWs depend on the treatment of convection in simulations of 5-km horizontal resolution. Our analysis is based on two 1-week simulations of the icosahedral nonhydrostatic (ICON) atmosphere model (Zängl et al., 2014). One simulation is performed with and the other one without a convective parameterization. We use the convection scheme of Bechtold et al. (2008), which is used and optimized for operational weather forecasts by the German Weather Service with 6.5- and 13-km horizontal grid spacings over Europe and surrounding regions, respectively. Thus, the convective parameterization is tuned for high resolution.

Comparisons with observations are carried out to ensure that the model simulations are broadly realistic. However, we do not present a detailed model evaluation. Section 2 introduces the simulations, observational data, and analysis methods. Results are presented in section 3, and a summary is given in section 4.

2. Data and Methods

2.1. Numerical Simulations

The model simulations are performed with the operational weather forecasting model ICON (Zängl et al., 2014) of the German Weather Service, which is jointly developed with the Max Planck Institute for Meteorology. In contrast to the operational configuration, a horizontal resolution of 5 km is used, and no subgrid parameterization for GW effects on the resolved flow is applied. As for the numerical weather forecasts, 90 levels are used in the vertical with a model top at 75 km. The vertical resolution in the stratosphere varies between 400 and 1,500 m. The Klemp-type Rayleigh damping (Klemp et al., 2008) of vertical winds starts at 44 km, above the levels analyzed in this study. Fast physics and tracer advection are computed every 45 s, convection every 630 s.

The model is run in two configurations, differing in their representation of convection. The first simulation, referred to as “PC” (for parameterized convection), uses a bulk mass-flux parameterization for moist convection (Bechtold et al., 2008; Tiedtke, 1989), and the second simulation, referred to as “EC” (for explicit convection), does not use any subgrid representation of moist convection. Thus, the only difference between EC and PC is the treatment of convection. GWs are not parameterized but explicitly generated in EC and PC, as both simulations couple temperature tendencies from condensation to the dynamic variables of the model.

Simulations are initialized from the operational analysis of the European Centre for Medium-Range Weather Forecasts (ECMWF) on the 1 August 2016. Sea surface temperatures are constant and based on the ECMWF reanalysis product at the initial time (1 August 2016, 00 UTC). Our study focuses on days 2 to 9 of the simulations. This is to avoid artifacts due to the initialization in the first hours of the simulations and to avoid a strong divergence of the atmospheric state between the two simulations and nature.

2.2. Observational Data

We use 30-min $0.1^\circ \times 0.1^\circ$ precipitation data from the Tropical Rainfall Measuring Mission (TRMM; Huffman et al., 2014) for a comparison of observed and simulated mean precipitation and precipitation variability in the tropics and subtropics.

The simulated GW momentum flux (GWMF) is compared to global maps of absolute GWMF at 30-km altitude provided by the gravity wave climatology based on atmospheric infrared limb emissions (GRACILE) climatology (Ern et al., 2018). GRACILE GWMF is derived from the satellite instruments High Resolution Dynamics Limb Sounder (HIRDLS) and Sounding of the Atmosphere using Broadband Emission Radiometry (SABER), both of which are infrared limb sounders. SABER measurements cover the altitude range 30–90 km, and HIRDLS covers 30–50 km. Vertical profiles of temperatures are retrieved along a track that is approximately parallel to the satellite track. Each vertical profile is used to estimate the amplitude and the vertical wavelength of the strongest wave component. The horizontal wavelength can be estimated from vertical phase shifts between consecutive profiles when they are spaced ≤ 300 km apart. For each pair of matching profiles, the GWMF is computed from the GW amplitude, vertical, and horizontal wavelength (Ern et al., 2004, 2011). The data are averaged over $15^\circ \times 5^\circ$ longitude-latitude boxes with steps of $5^\circ \times 2.5^\circ$ longitude-latitude for HIRDLS and $30^\circ \times 20^\circ$ longitude-latitude boxes with steps of $10^\circ \times 5^\circ$ longitude-latitude for SABER. Due to SABER's spatial sampling pattern, fewer pairs of vertical profiles are available for the computation of GWMF (Ern et al., 2018). This measurement technique is sensitive to GWs with horizontal wavelengths longer than ~ 100 – 200 km and vertical wavelengths longer than ~ 3 km. GWMF from GRACILE should be considered a lower bound of the true flux because the along-track estimates of horizontal wavelengths are greater or equal to the true horizontal wavelengths. Details of the measurement sensitivities are described in Ern et al. (2018).

August has the advantage of strong activity of convective GWs in the Northern Hemisphere subtropics, which is usually more pronounced than in the Southern Hemisphere subtropics during austral summer. Furthermore, SABER continuously observes high southern latitudes during this month and is thus able to capture GWs in the southern subpolar latitudes that primarily originate from orography, jets, and fronts. To be able to compare the ICON simulations to average August distributions of GWMF of both HIRDLS and SABER, we select the multiyear average August GW distributions of the GRACILE climatology, since HIRDLS does not cover the year 2016.

2.3. Wave Analysis of Model Data

The GW horizontal pseudo-momentum flux is a function of the background density ρ_0 , the Coriolis parameter f , the intrinsic frequency $\hat{\omega}$, and the three-dimensional wind velocity perturbations (u' , v' , w'),

$$(F_x, F_y) = \rho_0 \left(1 - \frac{f^2}{\hat{\omega}^2} \right) (\overline{u'w'}, \overline{v'w'}), \quad (1)$$

where overlines denote averages over at least one wavelength. The computation of the terms $\overline{u'w'}$ and $\overline{v'w'}$ requires a spectral analysis to determine the covariance of the respective wind components. This is not possible here because the temporal resolution of the model output greatly exceeds typical GW periods, which can be shorter than 10 min. We select an analysis method that permits the computation of GWMF at individual time steps. The small-volume few-wave decomposition technique (S3D; Lehmann et al., 2012) has several additional advantages over other common methods for extracting GW parameters, such as Fourier analysis. First, S3D output variables, such as the GWMF and wave vector, are not functions of spectral space but of physical space, providing local information on the GWs. Second, at each physical location the method focuses on the wave that explains the most variance in the local three-dimensional temperature perturbation field. In this sense S3D results are similar to the GRACILE climatology. The following computational steps are carried out at 6, 12, 18, and 24 UTC of each day:

1. Regridding: Three-dimensional wind and temperatures are interpolated from the ICON grid to levels with a 500-m vertical spacing, and to a $0.05^\circ \times 0.05^\circ$ latitude-longitude grid.
2. Background removal: Perturbation temperatures are obtained by removing zonal waves of wave numbers up to 18. In addition, we smooth the background by applying a Savitzky-Golay filter (Savitzky & Golay, 1964) in latitude and altitude direction based on third-order polynomials over 5° latitude and fourth-order polynomials over 5-km altitude. These choices are designed to eliminate most planetary waves and to focus the analysis on GWs. Sensitivity tests with cutoff wave numbers of 12 and 6, respectively, and no

additional smoothing showed negligible differences, indicating the robustness of our results to the choice of filtering and smoothing.

3. Cube subsets: As mentioned above, S3D is able to characterize the local properties of GWs. This is possible because the method is applied to data inside small cubes. The three-dimensional filtered array of temperature perturbations is split into subsets of cubes of 130-km width in the zonal and meridional directions and 12-km depth. The cubes are centered at 30-km altitude, such that the bottom of a cube is located well above the tropopause and the top is situated well below the sponge layer of the model. The cubes are placed every $0.5^\circ \times 0.5^\circ$ such that neighboring cubes overlap.
4. Sinusoidal fit: The S3D algorithm is applied to data inside each cube separately. The algorithm performs a three-dimensional sinusoidal fit to the temperature perturbations, maximizing the explained variance. Unlike spectral methods like Fourier transforms, vertical and horizontal wavelengths of the fitted waves can exceed the respective cube dimensions. Our choice of cube size focuses the analysis on waves of vertical wavelength ≤ 40 km and horizontal wavelength $\leq 1,300$ km. This spectral range is consistent with the GRACILE climatology. Our choice of cube size was informed by empirical values from previous studies (Krisch et al., 2017; Lehmann et al., 2012). Quantities derived from the wave fit include the GW amplitude \hat{T} and the zonal, meridional, and vertical wave numbers (k , l , and m). From these parameters GWMF is computed as

$$(F_x, F_y) = \frac{1}{2} \rho_0 \frac{(k, l)}{m} \left(\frac{g}{N} \right)^2 \left(\frac{\hat{T}}{T_0} \right)^2, \quad (2)$$

where g denotes the gravitational acceleration, N the buoyancy frequency, ρ_0 the background density, and T_0 the background temperature. Our assumption of upward wave propagation fixes the propagation direction of the wave.

5. Data collection: S3D results from all cubes are collected on a $0.5^\circ \times 0.5^\circ$ grid, corresponding to the spacing of the cubes.

To ensure that a different time sampling of the satellite and model data does not significantly change the results presented here, we repeated the analysis with composites created from identical local times. The resulting changes, which could in principle result from the existence of a diurnal cycle or a different viewing geometry on the ascending versus the descending branches of the satellites, were found to be only about 10% of the overall uncertainties.

3. Results

As the main focus here is on GWs generated by convection, we first examine convective sources in EC and PC in terms of precipitation rates. Despite having averaged over 7 days, we can still distinguish small-scale structures in the precipitation field of EC that are not present in PC (Figures 1b and 1c). For example, PC precipitation over Africa is spatially more coherent than EC or TRMM. In addition, PC lacks precipitation peaks in the tropical Indian Ocean and the northeastern Bay of Bengal (Figure 1d). The small areas of peak precipitation values in EC are indicative of strong rainfall events.

In addition to mean precipitation, we examine the standard deviation of 30-min precipitation rates (Figures 1e–1h). A larger standard deviation is associated with a more frequent occurrence of intense 30-min precipitation rates, and GWs are forced most strongly during the developing and mature stages of convection. Therefore, 30-min standard deviations serve as a good indicator of GW-generating convection. The standard deviation of precipitation in EC is much greater than in PC or TRMM observations, suggesting that convection is underresolved in EC; without a convective parameterization large instabilities are required to trigger convection in a column of the model. Therefore, at the relatively coarse resolution of 5 km, convection in EC occurs less frequently but is stronger than in PC or in observations. Although TRMM variability may be underestimated (Tan & Duan, 2017), variability in PC is even weaker than in TRMM, except for a narrow band of high standard deviation over Africa (Figure 1h). These findings suggest that EC may produce GWs of larger amplitudes compared to PC.

Before analyzing the simulated GWMF, it is instructive to examine Fourier power spectra of stratospheric winds (Figure 2). The 30-km spectra of EC and PC zonal winds exhibit the expected k^{-3} dependence at large scales (small zonal wave numbers) with a transition to a shallower slope, slightly steeper shallower than $k^{-\frac{5}{3}}$, at the mesoscale (Skamarock, 2004). The power spectra of vertical velocity are more or less flat in both

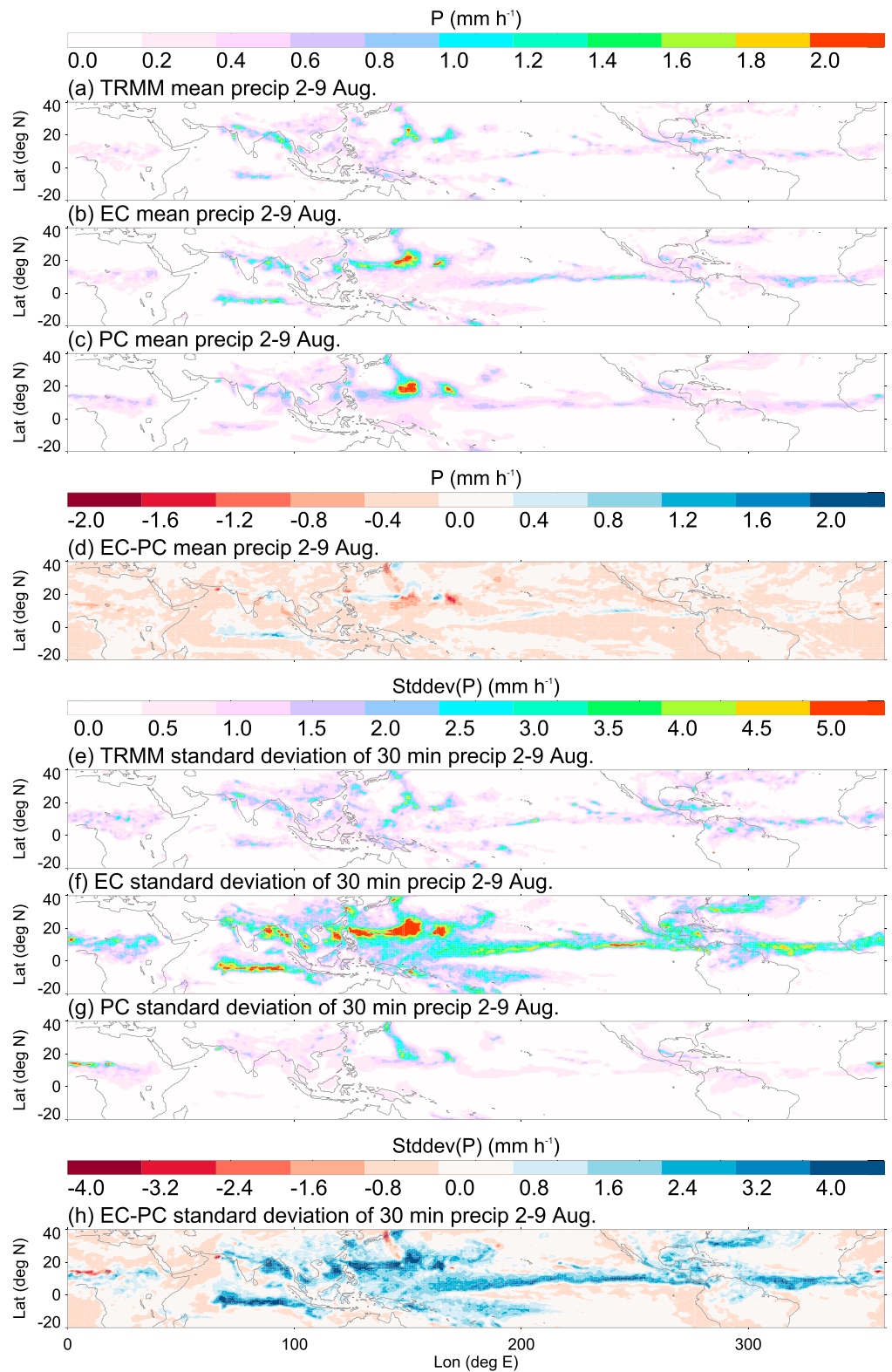


Figure 1. (a–c) Mean precipitation and (e–g) standard deviation of precipitation based on simulated (EC and PC) and observed (TRMM) 30-min data; (d) difference between (b) and (c); (h) difference between (f) and (g). TRMM = Tropical Rainfall Measuring Mission; EC = explicit convection; PC = parameterized convection.

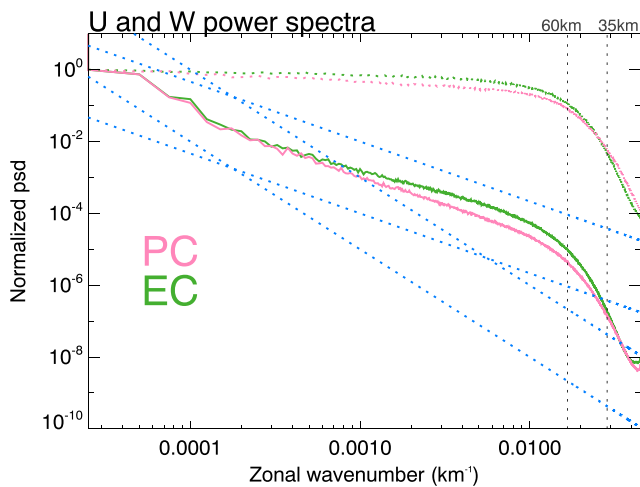


Figure 2. Fourier power spectra of simulated zonal winds (solid lines) and vertical winds (dotted lines) at 30-km averaged between 5° S and 5° N and normalized by their values at the shortest wave number. Wave numbers corresponding to wavelengths of 35 and 60 km are marked by black dashed lines. Blue dashed lines show slopes of $k^{-5/3}$ (shallow) and k^{-3} (steep). EC = explicit convection; PC = parameterized convection.

simulations. Dissipative mechanisms set in at large wave numbers, causing a rapid decay of energy at scales smaller than 12 times the grid scale. Thus, the simulations can be expected to resolve wavelengths ≥ 60 km. Moreover, EC has relatively more power at large wave numbers than PC. While the origin of the $k^{-5/3}$ slope is not fully understood at the mesoscale (Skamarock, 2004), GWs have been suggested as a contributing factor to explain this slope (Dewan, 1979; VanZandt, 1982). Therefore, the shallower spectrum in EC could result from an increased dominance of GWs at scales smaller than the mesoscale, as was also argued in Liu et al. (2014). The slope of the vertical velocity power spectrum is also shallower in EC. If this argument holds, then the energy spectra would imply more and/or stronger GWs in EC. Malardel and Wedi (2016) examined vertically integrated kinetic energy spectra in simulations with and without parameterized deep convection at 5- and 9-km horizontal resolutions performed with the hydrostatic Integrated Forecasting System (IFS) of the ECMWF. They also reported shallower slopes in the simulations that did not parameterize deep convection.

The time-averaged absolute GWMF at 30 km, derived from S3D, is indeed greater in EC than in PC. For a quantitative comparison of GWMF magnitudes, Figure 3a shows zonal mean values of simulated and observed GWMF. EC and PC agree well in the Southern Hemisphere, where convection is not the dominant source of GWs in August. This is expected

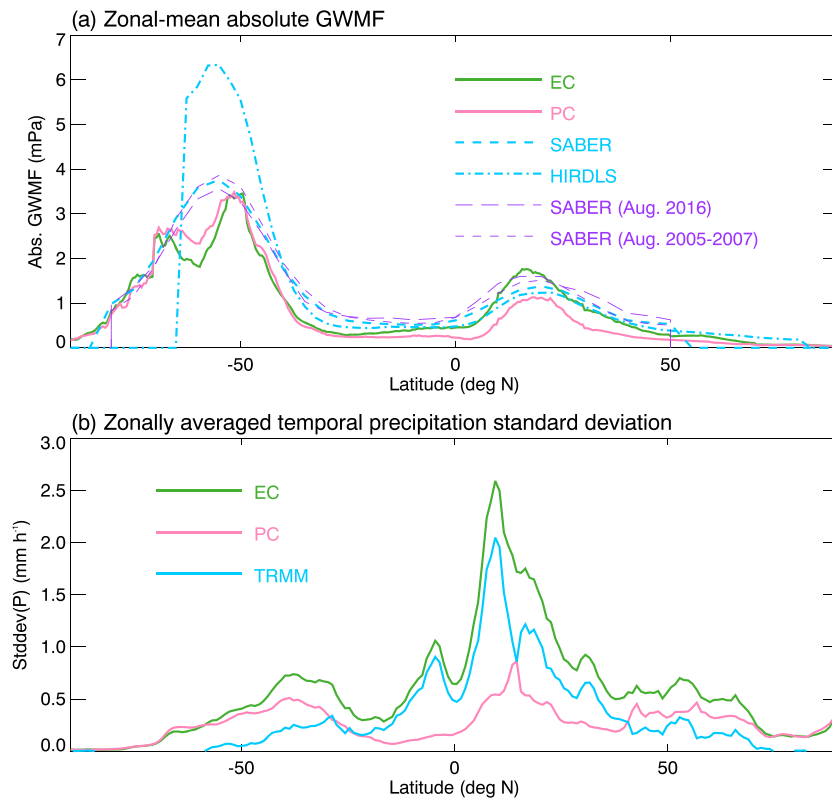


Figure 3. (a) Zonal-mean simulated GWMF and climatological August GWMF observed by SABER and HIRDLS from the GRACILE climatology at 30 km. August 2016 data are only shown for SABER, as they are not available from HIRDLS. Also shown are SABER data for the 2005–2007 HIRDLS period. (b) Zonal averages of the precipitation standard deviation shown in Figures 1e–1g. TRMM = Tropical Rainfall Measuring Mission; EC = explicit convection; PC = parameterized convection; GWMF = gravity wave momentum flux; SABER = Sounding of the Atmosphere using Broadband Emission Radiometry; HIRDLS = High Resolution Dynamics Limb Sounder.

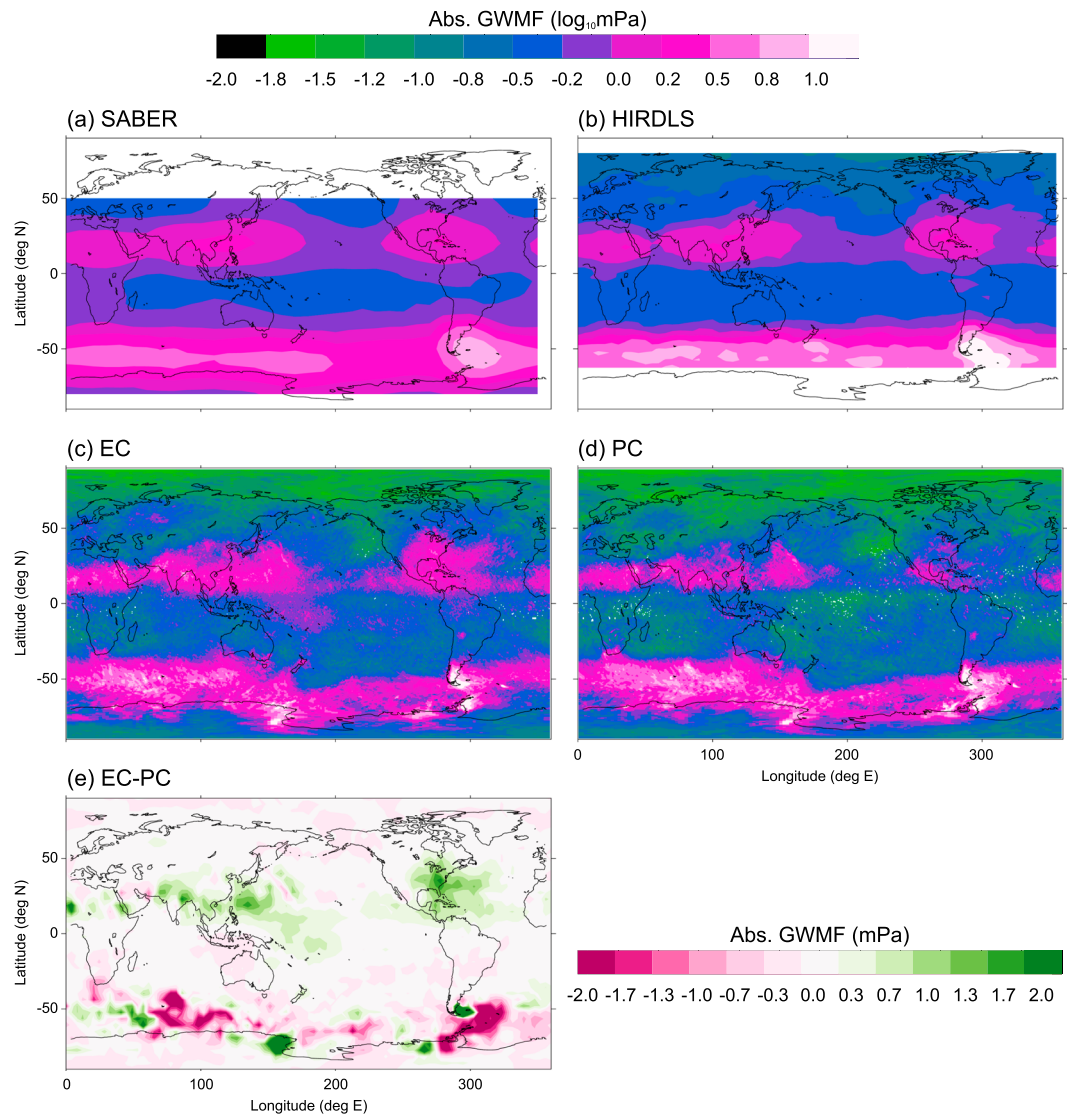


Figure 4. August absolute GWMF at 30 km observed by (a) SABER and (b) HIRDLS from the GRACILE climatology (plotted at the resolution of the GRACILE climatology; $10^\circ \times 5^\circ$ longitude-latitude for SABER and $5^\circ \times 2.5^\circ$ longitude-latitude for HIRDLS); (c and d) simulated absolute GWMF computed with S3D for 2–9 August 2016 (plotted at a resolution of $0.5^\circ \times 0.5^\circ$); (e) difference between (c) and (d). The horizontal resolution in (e) is reduced to $4^\circ \times 4^\circ$ to reduce graininess. EC = explicit convection; PC = parameterized convection; GWMF = gravity wave momentum flux; SABER = Sounding of the Atmosphere using Broadband Emission Radiometry; HIRDLS = High Resolution Dynamics Limb Sounder.

because the treatment of convection does not have a first-order impact on other GW exciting mechanisms. GWMF at 55° – 65° S is slightly greater in PC. However, our analysis is based on only 1 week, such that small differences in this region may be caused by few strong GW events related to jet instabilities or wind bursts over orography. At 55° – 65° S 1% of our S3D-derived GWMF data account for $\sim 26\%$ of the time mean zonal mean GWMF, and 0.1% of the data account for 9% of the GWMF. These values, which hold for EC and PC, are consistent with high-pressure balloon measurements from the Vorcore campaign and satellite observations at 50° – 65° S (Hertzog et al., 2012).

To the north of 20° S, in contrast, GWMF in EC is always ~ 30 – 50% greater than in PC. This is consistent with the greater precipitation variability in EC (Figure 3b). The secondary precipitation peak at $\sim 5^\circ$ S, which is seen in TRMM and EC, likely stems from the Indian Ocean (Figure 1). There is no evidence for a corresponding GWMF signature in Figure 3a, which is most likely a result of wind filtering. At 5° S zonal winds turn from easterly to westerly at ~ 22 -km altitude, whereas at 0 – 30° N easterly winds prevail from the surface

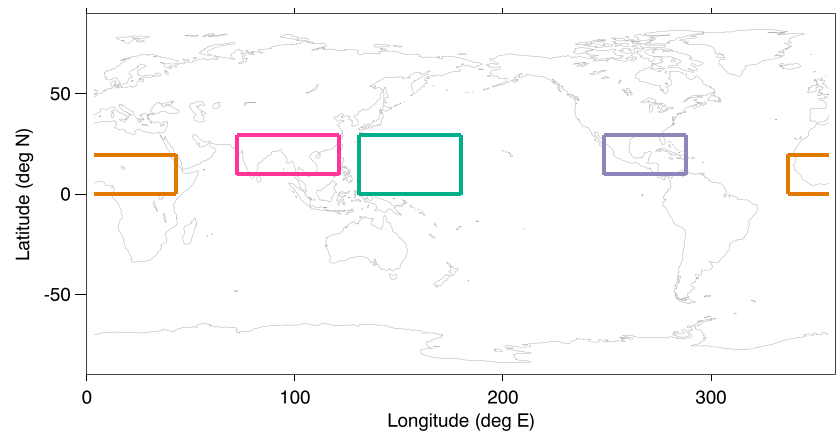


Figure 5. Latitude-longitude boxes chosen for a regional analysis of precipitation, vertical velocities, and gravity waves. The regions are selected to enclose areas of strong precipitation and are referred to as (left to right) the African Monsoon, the Asian Monsoon, the West Pacific, and Middle America.

up to 40 km. To exclude that differences between GWs in EC and PC result from different large-scale winds, we confirmed that differences in zonal-mean zonal winds between EC and PC are small, typically $<10\%$ (not shown). Both simulations reproduce the observed latitudinal variation of GWMF reasonably well. However, the comparison to satellites should be considered a qualitative one, as observations represent several years of August, whereas the model data consist of only 7 days. In the SABER data for August 2016, GWMF in the Southern Hemisphere polar vortex is $\sim 20\%$ lower on zonal average, while convective GWMF in the Northern Hemisphere subtropics is somewhat stronger. The greater GWMFs south of 50° S in HIRDLS compared to SABER result from HIRDLS's ability to sample shorter horizontal wavelengths and a favorable observational geometry at these latitudes. It is encouraging that ICON matches the observed latitudinal profiles without using any type of GW parameterization for unresolved waves.

Figures 4c and 4d show the global distributions of absolute GWMF at 30 km. It confirms the larger GWMF in EC in both the Northern Hemisphere midlatitudes and the tropics/subtropics (Figure 4e). At these latitudes convective sources are prevalent. The eastern United States, between the Gulf of Mexico and the Great Lakes, is one example of a region with little topography and substantial differences between the GWMF in EC and PC. This region is one of the four low-latitude hot spots in satellite measurements (Figures 4a and 4b); strong GWMF is also observed over the West Pacific, South Asia, and at 10° – 30° N over Africa. These hot spots can all be identified in EC and PC, with better-matching magnitudes in EC.

To examine simulated GW properties in greater detail, we now focus on the four regions of Figure 5, which are subjectively chosen to enclose areas of strong precipitation variability (cf. Figure 1). We will refer to them as the African Monsoon, the Asian Monsoon, the West Pacific, and Middle America, respectively. As expected from Figure 1f, strong precipitation rates occur more frequently in EC. In the Asian Monsoon, the West Pacific, and Middle America, precipitation rates exceeding 10 mm/hr are about 10 times more frequent in EC compared to PC (Figures 6d, 6f, and 6h). In the African Monsoon, the agreement between PC and EC is better, even though both simulations produce more frequently large precipitation events than observed by TRMM, which may point to a common bias in convection over land. This closer match of precipitation strengths over Africa between EC and PC may result from a stronger forcing of precipitation that could stem from orography or from a stronger diurnal cycle over land compared to the oceans. GWMF magnitudes are greater in EC than in PC in all four regions (Figures 6a, 6c, 6e, and 6g).

To confirm that surface precipitation rates have a direct impact on GWMF at 30-km altitude, which is well above the level of convective GW sources, Figures 7a and 7b examine the relationship between 15-min $5\text{ km} \times 5\text{ km}$ surface precipitation rates on tropospheric vertical velocities at altitudes of $z = 5, 10,$ and 15 km within the same vertical column. By standard thermodynamical arguments, stronger precipitation rates are associated with greater heating rates and greater vertical velocities. This is reflected in the monotonic increase of mean vertical velocities at $z = 5\text{ km}$ and $z = 10\text{ km}$ with increasing precipitation rates. At $z = 5\text{ km}$ EC simulates greater mean vertical velocities, but the vertical velocity statistics of EC and PC are similar in that there is substantial overlap of their interquartile ranges. At $z = 10\text{ km}$ the differences

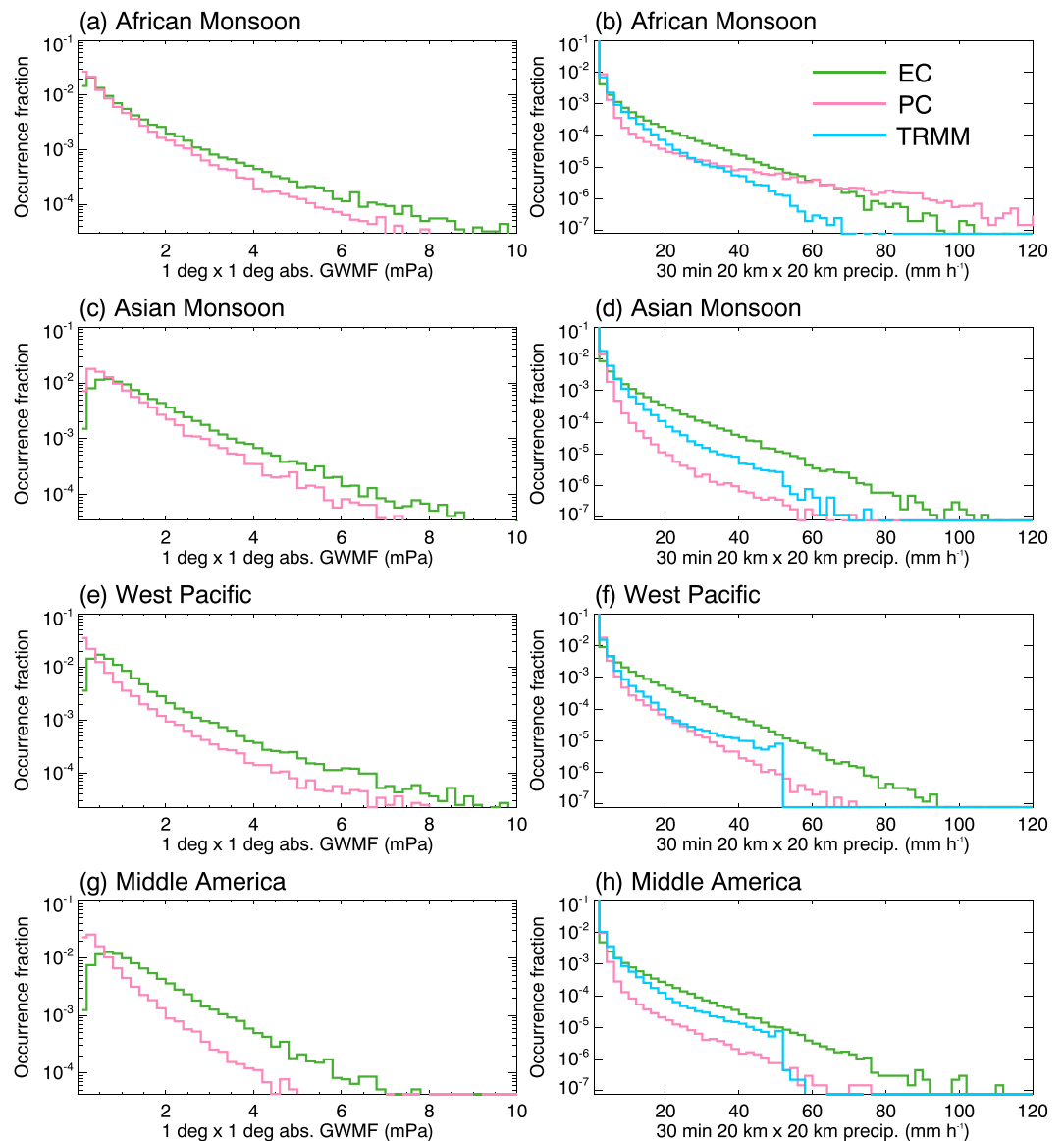


Figure 6. For the four regions shown in Figure 5, the occurrence fraction of (a, c, e, and g) $1^\circ \times 1^\circ$ absolute GWMF magnitudes at 30 km in EC and PC, and (b, d, f, and h) 30-min $20 \text{ km} \times 20 \text{ km}$ precipitation rates in EC, PC, and observations from TRMM. The scales for horizontal averaging are chosen to represent the typical horizontal scales of GWs and deep convection, respectively. The unphysical drop of the TRMM histograms at 50.8 mm/hr results from the processing of satellite data. Specifically, memory limitations made it necessary to encode values in the data format character, which created an artificial upper bound at 50.8 mm/hr. Thus, the drop only appears over the ocean and not over land, where rain gauges are included. GWMF = gravity wave momentum flux; TRMM = Tropical Rainfall Measuring Mission; EC = explicit convection; PC = parameterized convection.

between EC and PC are more pronounced. For a given precipitation rate, EC produces substantially greater vertical velocities. Values in the 99th percentile can reach $\sim 20 \text{ m/s}$ in EC. Resolved convective updrafts lead to higher vertical velocities in the upper troposphere in EC. Müller et al. (2018) also found that a convective parameterization in their idealized model with a 20-km grid spacing suppressed deep modes of tropical latent heating, which strongly supports our hypothesis. Large vertical velocities at $z = 15 \text{ km}$ could be associated with overshooting convection or with GWs. Both phenomena are affected by advection or lateral propagation, respectively, such that at $z = 15 \text{ km}$ a strong relationship between vertical velocities and precipitation is no longer found (Figure 7c).

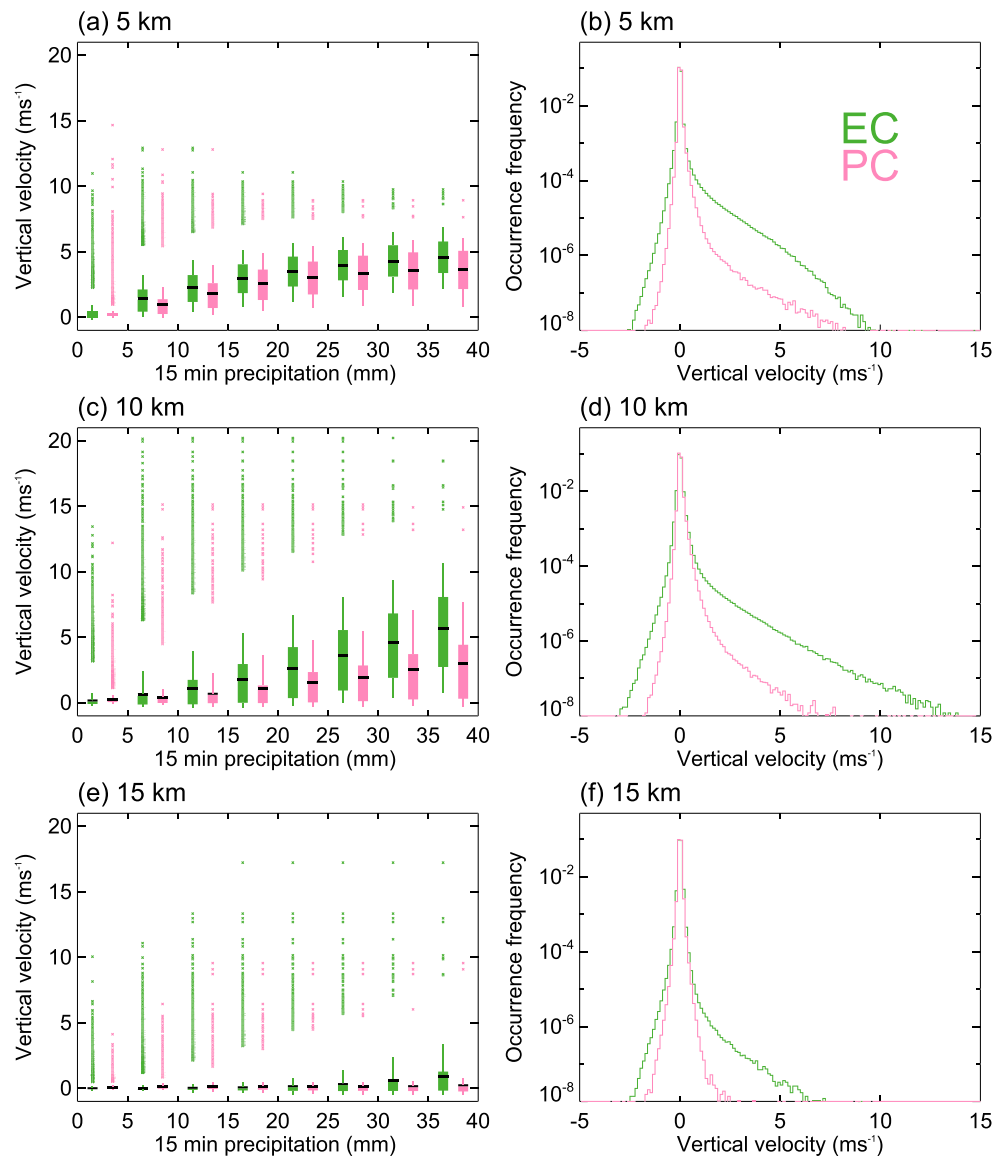


Figure 7. (a,c, and e) The relationship between simulated vertical velocities at altitudes of 5, 10, and 15 km, respectively, with surface precipitation rates. Data are based on 5 km × 5 km grid boxes at 0°–30°N. The 15-min periods of precipitation accumulation precede the times at which vertical velocity distributions are computed. Data are binned into 5-mm precipitation intervals to compute statistical properties of vertical velocity: average (black horizontal line), interquartile range (box), 10th and 90th percentile (vertical lines), and outliers within the 99th percentile (dots). (b,d, and f) Occurrence frequencies of vertical velocities at altitudes of 5, 10, and 15 km, respectively, also based on 5 km × 5 km data at 0°–30° N. EC = explicit convection; PC = parameterized convection.

The stronger vertical velocities in EC (Figure 7) combined with the more frequent occurrence of strong precipitation rates in EC (Figures 6b, 6d, 6f, and 6h) explain the increased occurrence of large vertical velocities at 5- and 10-km altitude (Figures 7b and 7d), which are still found at 15 km (Figure 7f). These are indicative of stronger GW sources in EC. Yet differences at the source level may not necessarily translate into differences at 30 km. Wave propagation could differ between the four focus regions or between the simulations if the background wind profiles were sufficiently different. However, the simulated zonal wind profiles are very similar between the four regions (Figure 8a; note that the curves in Figure 8a are offset by 1 m/s). In addition, PC and EC simulate nearly identical zonal wind profiles for each region (Figure 8b; note that the curves in Figure 8b are offset by 0.1 m/s). Because of the vertical extent of the S3D cubes, GWMF cannot be computed at low altitudes. Thus, to approximate GWMF we compute the vertical profiles of the zonal mean zonal momentum flux $F_x = \rho_0 \overline{u'w'}$ from 20 km upward (Figure 8c). F_x decreases with altitude at nearly

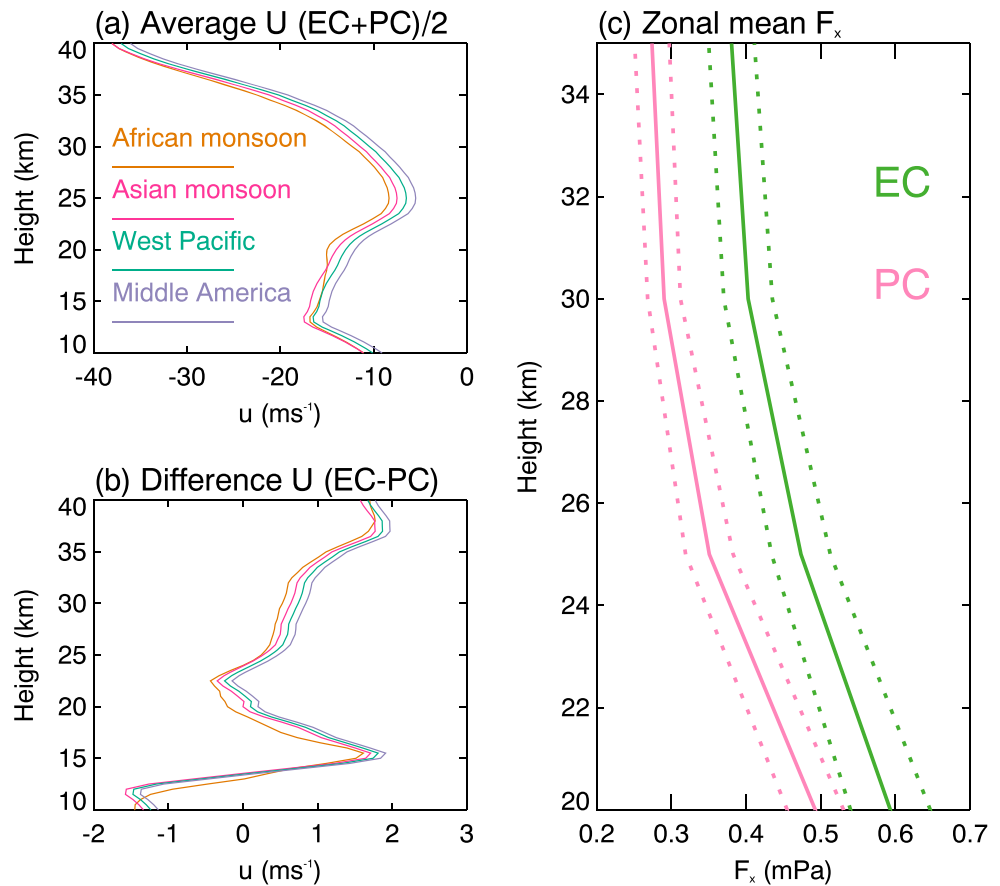


Figure 8. (a and b) Vertical profiles of zonal wind for the four regions shown in Figure 5. (a) The average of EC and PC (curves are offset by 1 m/s); (b) the difference between the EC and PC (curves are offset by 0.1 m/s). (c) Vertical profiles of zonal mean zonal momentum flux $F_x = \rho_0 u' w'$ computed every 5-km altitude, averaged between 0° and 30°N . ρ_0 is the background density, and (u', w') is computed from data with a horizontal resolution of $100 \text{ km} \times 100 \text{ km}$ with variability at scales $>1,000 \text{ km}$ removed. EC = explicit convection; PC = parameterized convection.

identical rates in EC and PC. This provides further evidence that differences in GWMF at 30 km are not strongly affected by GW propagation but originate from different convective properties in EC and PC.

Figure 9 shows the spectral distribution of GWMF inside each region as a function of wave propagation direction and ground-based phase speed. The number next to each panel gives the average GWMF inside each region in units of millipascals. Each plot is normalized to allow for a comparison of the shape of the spectra. The average GWMF in EC is ~ 30 – 100% greater than in PC, as one may expect from Figures 6a, 6c, 6e, and 6g. The spectra between EC and PC do not only differ in terms of their amplitude, but also in terms of their spectral distribution. Spectra in EC are broader in both phase speed and propagation direction. Thus, at 30-km EC is associated with relatively more fast waves and more northward, southward, and westward, instead of mainly eastward propagation, with again the exception of the African Monsoon. EC closely matches the satellite-derived GWMF magnitudes; deviations from SABER are $<7\%$ and deviations from HIRDLS are $<5\%$ with the exception of the West Pacific (right-hand side of Figure 9). GWMF magnitudes in PC are everywhere much smaller than the satellite-derived values.

The shift to higher phase speeds in EC is consistent with the higher temporal variability of precipitation in EC (Figure 1). Linear theory predicts that deeper convection triggers broader spectra of GWs with peaks at relatively higher phase speeds. In addition, broader spectra are associated with convection that is more confined in its horizontal extent (Beres et al., 2004, 2005). Our analysis of precipitation characteristics in EC and PC is consistent with more intense and spatially confined convection in EC. Thus, the different treatment of convection between the two simulations is associated with changes in the morphology of typical GW generating clouds.

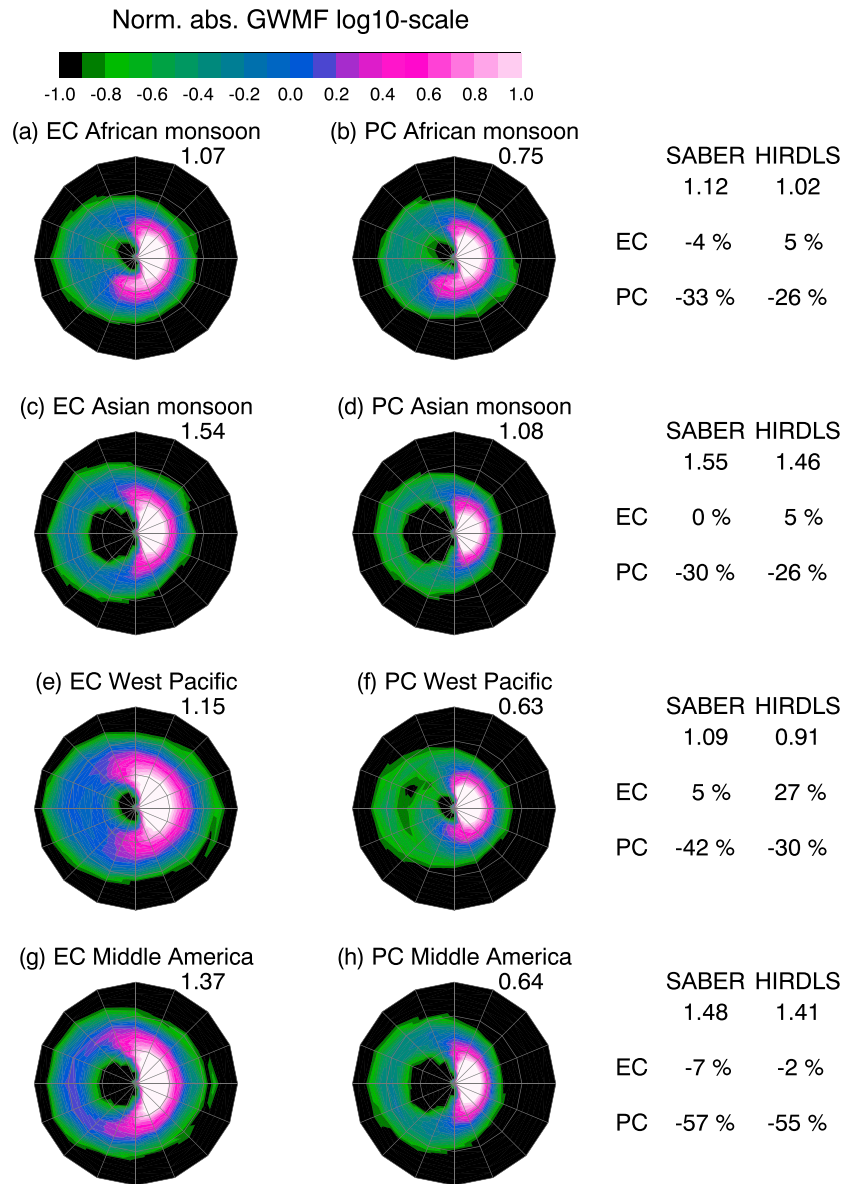


Figure 9. GWMF as a function of phase speed (radius; 5 m/s bins, spider-web circles mark 30, 60, and 90 m/s, respectively) and propagation direction (angle; 16 directions, east is to the right). GWMFs in each region are normalized by their totals. Numbers above each diagram give the average GWMF at 30 km inside each region in units of megapascals. Tables on the right-hand side show the average GWMF at 30 km observed by SABER and HIRDLS from the GRACILE climatology in units of megapascals (top row), and the deviations of the simulate GWMFs from this satellite climatology (in percent). EC = explicit convection; PC = parameterized convection; GWMF = gravity wave momentum flux; SABER = Sounding of the Atmosphere using Broadband Emission Radiometry; HIRDLS = High Resolution Dynamics Limb Sounder.

4. Conclusions

We analyze the differences between stratospheric GWs in two global simulations of 1 week of August with a horizontal grid spacing of 5 km. One simulation parameterizes convection (referred to as PC); the other does not (referred to as EC). EC is associated with greater precipitation variability; in PC strong precipitation events occur less frequently. Consistent with stronger convective GW sources in the Northern Hemisphere subtropics, where convection is the dominant source of GWs, zonal mean absolute GWMF is ~30–50% greater in the explicit simulation, while regional differences can reach ~100%. The GWMF spectrum associated with EC is broader in terms of wave amplitude, phase speed, and propagation direction. We argue that this is due to stronger, deeper, and more spatially confined heating in the explicit simu-

lation. The relationship between local vertical velocities and surface precipitation reveals the presence of stronger updrafts in EC, particularly in the upper troposphere, which supports this argument. Overall, the treatment of convection has a substantial impact on the generated GWs. Using explicit versus parameterized convection mainly changes the magnitude of absolute GWMF, and this change depends on latitude. These aspects need to be considered when climate models are set up to operate at convection-permitting resolution. Lastly, it is promising that both configurations of the ICON model considered here are able to reproduce satellite-derived GWMF patterns without using additional parameterizations for unresolved GWs. Over the Northern Hemisphere monsoon regions, GWMF magnitudes in the simulation with explicit convection match those derived from SABER and HIRDLS within 7%. GWMF magnitudes in the run with parameterized convection are everywhere much smaller than the satellite-derived values. However, a large fraction of the GWMF is expected to be associated with small-scale waves. Thus, since neither observations nor models cover horizontal wavelengths below ~ 50 km, the results obtained here do not imply that GW parameterizations are dispensable.

Acknowledgments

The work of C. C. Stephan and H. Schmidt was supported by the Deutsche Forschungsgemeinschaft (DFG, German Research Foundation) project SCHM 2158/5-2, which is part of the DFG researcher group FOR 1898 (MS-GWaves). The work of M. Ern, P. Preusse, and C. Strube was supported by the DFG projects ER 474/4-2 and PR 919/4-2 (MS-GWaves/SV), which are also part of MS-GWaves. The GPM IMERG Final Precipitation data were provided by the NASA/Goddard Space Flight Center's Precipitation Processing System, which develop and compute the GPM IMERG Final Precipitation as a contribution to the Global Precipitation Measurement (GPM) mission, and are archived at the NASA GES DISC, doi: <https://doi.org/10.5067/GPM/IMERG/3B-MONTH/05>. We would like to thank David Bolvin from the IMERG team for helping us understand the TRMM data shown in Figure 6, and Stefan Kinne and Christian Kummerow for contacting him on our behalf. The GRACILE data set is available at <https://doi.org/10.1594/PANGAEA.879658>. Data from numerical simulations are stored by the Excellence in Science of Weather and Climate in Europe (ESiWACE) project at the German Climate Computing Center (DKRZ) and can be made available upon request. We thank the HIRDLS and SABER instrument teams for creating and maintaining the satellite data sets. HIRDLS level 2 data are freely available via the NASA Goddard Earth Sciences Data and Information Services Center (GES DISC) at <http://disc.sci.gsfc.nasa.gov/Aura>. SABER data are provided by GATS Inc. and are freely available at <http://saber.gats-inc.com/>.

References

- Bacmeister, J. T., Wehner, M. F., Neale, R. B., Gettelman, A., Hannay, C., Lauritzen, P. H., et al. (2014). Exploratory high-resolution climate simulations using the community atmosphere model (CAM). *Journal of Climate*, *27*, 3073–3099.
- Bechtold, P., Köhler, M., Jung, T., Doblas-Reyes, F., Leutbecher, M., Rodwell, M., et al. (2008). Advances in simulating atmospheric variability with the ECMWF model: From synoptic to decadal time-scales. *Quarterly Journal of the Royal Meteorological Society*, *134*, 1337–1351.
- Beres, J. H., Alexander, M. J., & Holton, J. R. (2004). A method of specifying the gravity wave spectrum above convection based on latent heating properties and background wind. *Journal of the Atmospheric Sciences*, *61*, 324–337.
- Beres, J. H., Garcia, R. R., Boville, B. A., & Sassi, F. (2005). Implementation of a gravity wave source spectrum parameterization dependent on the properties of convection in the Whole Atmosphere Community Climate Model. *Journal of Geophysical Research*, *110*, D10108. <https://doi.org/10.1029/2004JD005504>
- Choi, H.-J., & Chun, H.-Y. (2011). Momentum flux spectrum of convective gravity waves. Part I: An update of a parameterization using mesoscale simulations. *Journal of the Atmospheric Sciences*, *68*(4), 739–759.
- Dewan, E. M. (1979). Stratospheric spectra resembling turbulence. *Science*, *402*, 832–835.
- Ern, M., Preusse, P., Alexander, M. J., & Warner, C. D. (2004). Absolute values of gravity wave momentum flux derived from satellite data. *Journal of Geophysical Research*, *109*, D20103. <https://doi.org/10.1029/2004JD004752>
- Ern, M., Preusse, P., Gille, J. C., Hepplewhite, C. L., Mlynarczyk, M. G., Russell, J. M. III, & Riese, M. (2011). Implications for atmospheric dynamics derived from global observations of gravity wave momentum flux in stratosphere and mesosphere. *Journal of Geophysical Research*, *116*, D19107. <https://doi.org/10.1029/2011JD015821>
- Ern, M., Trinh, Q. T., Preusse, P., Gille, J. C., Mlynarczyk, M. G., Russell, J. M. III, & Riese, M. (2018). GRACILE: A comprehensive climatology of atmospheric gravity wave parameters based on satellite limb soundings. *Earth System Science Data*, *10*, 857–892.
- Garcia, R. R., Smith, A. K., Kinnison, D. E., de la Camara, A., & Murphy, D. J. (2017). Modification of the gravity wave parameterization in the Whole Atmosphere Community Climate Model: Motivation and results. *Journal of the Atmospheric Sciences*, *74*(1), 275–291.
- Gelaro, R., & Coauthors, A. (2015). Evaluation of the 7 km GEOS-5 nature run (NASA/TM-2014-104606). Greenbelt, MD: NASA, Goddard Space Flight Center, Technical report series on global modeling and data assimilation (Vol. 36, pp. JPI.7).
- Geller, M. A., Alexander, M. J., Love, P. T., Bacmeister, J., Ern, M., Hertzog, A., et al. (2013). A comparison between gravity wave momentum fluxes in observations and climate models. *Journal of Climate*, *26*, 6383–6405.
- Hertzog, A., Alexander, M. J., & Plougonven, R. (2012). On the intermittency of gravity wave momentum flux in the stratosphere. *Journal of the Atmospheric Sciences*, *69*(11), 3433–3448.
- Holt, L. A., Alexander, M. J., Coy, L., Liu, C., Molod, A., Putman, W., & Pawson, S. (2017). An evaluation of gravity waves and gravity sources in the southern hemisphere in a 7 km global climate simulation. *Quarterly Journal of the Royal Meteorological Society*, *143*, 2481–2495.
- Huffman, G., Bolvin, D., Braithwaite, D., Hsu, K., Joyce, R., & Xie, P. (2014). In tegrated Multi-satellitE Retrievals for GPM (IMERG). version 4.4. NASA's Precipitation Processing Center.
- Kim, Y. H., Bushell, A. C., Jackson, D. R., & Chun, H.-Y. (2013). Impacts of introducing a convective gravity-wave parameterization upon the QBO in the Met Office Unified Model. *Geophysical Research Letters*, *40*, 1873–1877. <https://doi.org/10.1002/grl.50353>
- Kim, S.-Y., Chun, H.-Y., & Baik, J.-J. (2007). Sensitivity of typhoon-induced gravity waves to cumulus parameterizations. *Geophysical Research Letters*, *34*, L15814. <https://doi.org/10.1029/2007GL030592>
- Klemp, J. B., Dudhia, J., & Hassiotis, A. D. (2008). An upper gravity-wave absorbing layer for NWP applications. *Monthly Weather Review*, *136*, 3987–4004.
- Krisch, I., Preusse, P., Ungermann, J., Dörnbrack, A., Eckermann, S. D., Ern, M., et al. (2017). First tomographic observations of gravity waves by the infrared limb imager GLORIA. *Atmospheric Chemistry and Physics*, *17*, 14,937–14,953.
- Lehmann, C. I., Kim, Y.-H., Preusse, P., Chun, H.-Y., Ern, M., & Kim, S.-Y. (2012). Consistency between Fourier transform and small-volume few-wave decomposition for spectral and spatial variability of gravity waves above a typhoon. *Atmospheric Measurement Techniques*, *5*, 1637–1651.
- Liu, H.-L., McInerney, J. M., Santos, S., Lauritzen, P. H., Taylor, M. A., & Pedatella, N. M. (2014). Gravity waves simulated by high-resolution Whole Atmosphere Community Climate Model. *Geophysical Research Letters*, *41*, 9106–9112. <https://doi.org/10.1002/2014GL02468>
- Lott, F., & Miller, M. J. (1997). A new subgrid-scale orographic drag parametrization: Its formulation and testing. *Quarterly Journal of the Royal Meteorological Society*, *123*, 101–127.
- Malardel, S., & Wedi, N. P. (2016). How does subgrid-scale parametrisation influence non-linear spectral energy fluxes in global NWP models? *Journal of Geophysical Research: Atmospheres*, *121*, 5395–5410. <https://doi.org/10.1002/2015JD023970>
- McFarlane, N. A. (1987). The effect of orographically excited gravity wave drag on the general circulation of the lower stratosphere and troposphere. *Journal of the Atmospheric Sciences*, *44*, 1775–1800.

- Müller, S. K., Manzini, E., Giorgetta, M. A., Sato, K., & Nasuno, T. (2018). Convectively generated gravity waves in high resolution models of tropical dynamics. *Journal of Advances in Modeling Earth Systems*, *10*, 2564–2588. <https://doi.org/10.1029/2018MS001390>
- Orr, A., Bechtold, P., Scinocca, J., Ern, M., & Janiskova, M. (2010). Improved middle atmosphere climate and forecasts in the ECMWF model through a nonorographic gravity wave drag parameterization. *Journal of Climate*, *23*, 5905–5926.
- Piani, C., Durran, D., Alexander, M. J., & Holton, J. R. (2000). A numerical study of three-dimensional gravity waves triggered by deep tropical convection and their role in the dynamics of the QBO. *Journal of the Atmospheric Sciences*, *57*, 3689–3702.
- Plougonven, R., & Zhang, F. (2014). Internal gravity waves from atmospheric jets and fronts. *Reviews of Geophysics*, *52*, 33–76. <https://doi.org/10.1002/2012RG000419>
- Prein, A. F., Langhans, W., Fossier, G., Ferrone, A., Ban, N., Goergen, K., et al. (2015). A review on regional convection-permitting climate modeling: Demonstrations, prospects, and challenges. *Reviews of Geophysics*, *53*, 323–361. <https://doi.org/10.1002/2014RG000475>
- Preusse, P., Ern, M., Bechtold, P., Eckermann, S. D., Kalisch, S., Trinh, Q. T., & Riese, M. (2014). Characteristics of gravity waves resolved by ECMWF. *Atmospheric Chemistry and Physics*, *14*(19), 10,483–10,508.
- Richter, J. H., Sassi, F., & Garcia, R. R. (2010). Toward a physically based gravity wave source parameterization in a general circulation model. *Journal of the Atmospheric Sciences*, *67*, 136–156.
- Savitzky, A., & Golay, M. J. E. (1964). Smoothing and differentiation of data by simplified least squares procedures. *Analytical Chemistry*, *36*(8), 1627–1639.
- Skamarock, W. C. (2004). Evaluating mesoscale NWP models using kinetic energy spectra. *Monthly Weather Review*, *132*, 3019–3032.
- Song, I.-S., & Chun, H.-Y. (2005). Momentum flux spectrum of convectively forced internal gravity waves and its application to gravity wave drag parameterization. Part I: Theory. *Journal of the Atmospheric Sciences*, *62*, 107–124.
- Stephan, C. C., & Alexander, M. J. (2015). Realistic simulations of atmospheric gravity waves over the continental U.S. using precipitation radar data. *Journal of Advances in Modeling Earth Systems*, *7*, 823–835. <https://doi.org/10.1002/2014MS000396>
- Tan, M. L., & Duan, Z. (2017). Assessment of GPM and TRMM precipitation products over Singapore. *Remote Sensing*, *9*, 720.
- Tiedtke, M. (1989). A comprehensive mass flux scheme for cumulus parameterization in large-scale models. *Monthly Weather Review*, *117*, 1779–1800.
- VanZandt, T. E. (1982). A universal spectrum of buoyancy in the atmosphere. *Geophysical Research Letters*, *9*, 575–578.
- Watanabe, S., Kawatani, Y., Tomikawa, Y., Miyazaki, K., Takahashi, M., & Sato, K. (2008). General aspects of a T213L256 middle atmosphere general circulation model. *Journal of Geophysical Research*, *113*, D12110. <https://doi.org/10.1029/2008JD010026>
- Zängl, G., Reinert, D., Ripodas, P., & Baldauf, M. (2014). The ICON (ICOSahedral Non-hydrostatic) modelling framework of DWD and MPI-M: Description of the non-hydrostatic dynamical core. *Quarterly Journal of the Royal Meteorological Society*, *141*, 563–579.